Environmental Science & Technology

Article

Cite This: *Environ. Sci. Technol.* 2019, 53, 13636−13647

pubs.acs.org/est

Ferrihydrite Growth and Transformation in the Presence of Ferrous Iron and Model Organic Ligands

Laurel K. ThomasArrigo,*[,†] Ralf Kaegi,[‡] and Ruben Kretzschmar[†]

[†]Soil Chemistry Group, Institute of Biogeochemistry and Pollutant Dynamics, Department of Environmental Systems Science, ETH Zurich, Universitätstraße 16, CHN, CH-8092 Zurich, Switzerland

[‡]Eawag, Swiss Federal Institute of Aquatic Science and Technology, Überlandstraße 133, CH-8600 Dübendorf, Switzerland

Supporting Information

ABSTRACT: Ferrihydrite (Fh) is a poorly crystalline Fe(III)-oxyhydroxide found in abundance in soils and sediments. With a high specific surface area and sorption capacity at circumneutral pH, ferrihydrite is an important player in the biogeochemical cycling of nutrients and trace elements in redox-dynamic environments. Under reducing conditions, exposure to Fe(II) induces mineral transformations in ferrihydrite; the extent and trajectory of which may be greatly influenced by organic matter (OM). However, natural OM is heterogeneous and comprises a range of molecular weights (MWs) and varied functional group compositions. To date, the impact that the chemical composition of the associated OM has on Fe(II)-catalyzed mineral transformations is not clear. To address this knowledge gap, we coprecipitated ferrihydrite with model organic ligands selected to cover a range of MWs (25 000−50 000 vs <200 Da) as well as carboxyl content (polygalacturonic acid (PGA) > citric acid (CA) > galacturonic acid (GA)). Coprecipitates (C:Fe ≈ 0.6) were reacted with 1 mM ^{57}Fe(II) for 1 week at pH 7, with time-resolved solid-phase analysis (via X-ray diffraction, X-ray absorption spectroscopy, and electron microscopy) revealing that all ligands inhibited Fe(II)-catalyzed ferrihydrite mineral transformations and the formation of crystalline secondary mineral phases compared to a pure ferrihydrite. For carboxyl-rich coprecipitates (Fh-PGA and Fh-CA), mineral transformations were less inhibited than in the carboxyl poor Fh-GA, and a crystalline lepidocrocite "shell" was formed surrounding the residual ferrihydrite core. However, Fe isotope analysis revealed that all coprecipitates underwent near complete atom exchange. Collectively, our results highlight that ferrihydrite is indeed an active mineral phase in redox-dynamic environments, but that its stability under reducing conditions, and thus capacity for nutrient and trace element retention, depends on the chemical characteristic of the associated OM, specifically OM-induced changes in the particle surface charge and the distribution of organic functional groups.

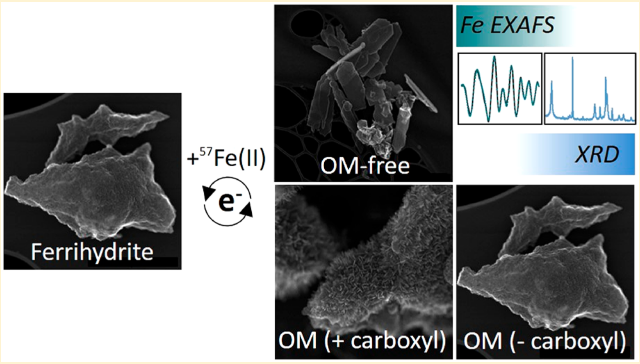

■ INTRODUCTION

Ferrihydrite, a poorly crystalline Fe(III)-oxyhydroxide, commonly occurs as a major Fe phase in natural soils. Owing to its high specific surface area (SSA) and sorption capacity under (sub)oxic conditions, and its tendency to undergo reductive dissolution and mineral transformation under reducing conditions, ferrihydrite plays an integral role in the biogeochemical cycling of nutrients and trace metal(loid)s, particularly in redox-dynamic environments like wetlands, riparian zones, and upper sediment layers. In such natural environments, pure mineral phases rarely occur, as the presence of dissolved organic matter (OM) often leads to the formation of ferrihydrite-OM coprecipitates that vary in structure and microbial- and geochemical-reactivity compared to pure mineral phases.[1−5]

With growing global interest in soil carbon sequestration, many studies have considered the mechanisms by which association with ferrihydrite stabilizes OM. Under oxic conditions, occlusion of OM in mineral-aggregate structures hinders biodegradation and mineralization of organic C,[6] while in the absence of O_2, Fe(III) acts as an electron acceptor, releasing solid-associated OM during the dissolution, recrystallization, and transformation of ferrihydrite.[7] However, recent works suggest that in the presence of dissolved ferrous Fe (Fe(II)), OM-associated ferrihydrite undergoes less mineral transformation than pure ferrihydrite.[8−12] Early studies suggested that the OM-associated ferrihydrite was entirely stable, undergoing neither recrystallization nor atom exchange.[11,13] However, with the application of stable iron isotopes as tracers, we now know that OM-associated ferrihydrite is dynamic; actively partaking in iron atom

Received: July 3, 2019
Revised: October 28, 2019
Accepted: October 29, 2019
Published: November 13, 2019

DOI: 10.1021/acs.est.9b03952

exchange and recrystallization, but that the presence of OM inhibits transformation to crystalline mineral phases.[8,9,12] Because the stabilization of high surface area ferrihydrite under reducing conditions has implications for the release of associated OM, elucidating the mechanics of how OM inhibits crystalline mineral formation in the presence of ferrous iron is important. Reactions between ferrihydrite and Fe(II) involve adsorption and oxidation of Fe(II) on the mineral surface followed by electron transfer; therefore, proposed mechanisms to explain this include the complete blockage of ferrihydrite surface sites by OM, or the preferential complexation of Fe(II) by OM.[9,11] However, recent research has shown that neither of these arguments can fully account for a lack of crystalline secondary mineral formation: For example, although no ferrihydrite mineral transformations were recorded in Fe-rich, organic flocs during reactions with Fe(II),[8,9] near complete transformation of ferrihydrite occurred in flocs exposed to S(-II).[14] Sulfidization also involves mineral surface-based electron transfer,[15] indicating that the floc-OM could not have blocked all surface sites. In addition, while complexation of Fe(II) with carboxyl groups of the OM may remove some Fe(II) from solution, carboxyl-rich surfaces may also be important to template the growth of high aspect-ratio crystalline minerals.[16−18] Moreover, our previous works showed that, in reactions between ferrihydrite-OM coprecipitates and Fe(II), despite the formation of OM-associated Fe(II), aqueous Fe(II) was not depleted and extensive iron atom exchange still occurred.[8,9]

Most recently, it was suggested that OM inhibits ferrihydrite growth via Ostwald ripening[19] and/or oriented aggregation;[8] both being hindered by changes in the surface charge of the coprecipitate compared to the pure mineral phase and by surface organic functional groups, which constrain the free movement and alignment of ferrihydrite nanoparticles. Highlighting this, Zhou et al.[12] showed that, upon exposure to Fe(II), ferrihydrite coprecipitated with a low molecular weight (LMW) fulvic acid showed less mineral transformation than a high molecular weight (HMW) humic acid coprecipitate, and suggested that the higher charge density of the LMW fulvic acid more effectively inhibited Ostwald ripening. However, the impact that diverse OM has on the resulting ferrihydrite nanoparticles in a coprecipitate is inherently more complex. In addition to the changes in surface charge resulting from ferrihydrite coprecipitation with OM of different molecular weight (MW),[12] varying the functional group population and position as well as the total C content may lead to significant structural differences in the coprecipitates, resulting in varied particle size, SSA, micro- and mesoporosity, and extent of structural distortion in the resulting ferrihydrite nanoparticles.[1,2,5,11,20,21] For determining iron atom exchange kinetics, any combination of these factors may be of influence. For example, in crystalline minerals such as lepidocrocite, goethite, or hematite, the effects of varied particle size[22−24] and OM type[25] have been shown to impact not only Fe(II)-catalyzed iron atom exchange kinetics,[22,23,25] but also the particle size of the transformation product.[22,23] However, such information is missing for ferrihydrite, where the majority of studies have included single OM type[8−11,13] or have limited solid-phase structural characterization data.[12,26]

Without comprehensive structural characterization of ferrihydrite nanoparticles in the initial coprecipitates, the effects of OM carboxyl content and charge density[12] on Fe(II) interactions with ferrihydrite-OM coprecipitates are indistinguishable from the impacts of structural variations in the ferrihydrite nanoparticles acquired during coprecipitation (e.g., increased structural distortion, varying particle size, and SSA). Therefore, in this study, we utilized extensive solid-phase characterization techniques (synchrotron X-ray techniques, X-ray diffraction, and electron microscopy) and employed stable isotope tracers to follow the recrystallization and transformation of ferrihydrite in ferrihydrite-OM coprecipitates during reactions with dissolved Fe(II), paying special attention to changes in the structural disorder, particle size, and bulk morphology of both the unreacted ferrihydrite-OM coprecipitates as well as Fe(II)-induced secondary mineral phases. Specifically, ferrihydrite was coprecipitated with polygalacturonic, galacturonic, and citric acid; model organic ligands chosen to address a range of MW (25000−50000 vs <200 Da) and, by extension, charge density,[12] as well as potential changes in particle surface charge via functional groups (e.g., carboxyl content). Coprecipitates were then reacted with 1 mM ^{57}Fe(II) for 1 week at pH 7, with time-resolved solid- and aqueous-phase analyses revealing competing growth mechanisms dependent upon OM carboxyl content and nanoparticle structure.

■ MATERIALS AND METHODS

Selection of Organic Acids. To assess the impact that MW, carboxyl-group content, and charge characteristics of the coprecipitating organic ligand exerts on Fe(II)-catalyzed transformations of ferrihydrite, reaction kinetics, and transformation products of a pure ferrihydrite were compared to those of ferrihydrite-OM coprecipitates comprising the model organic ligands polygalacturonic acid (PGA), galacturonic acid (GA), and citric acid (CA) (Figure S1 of the Supporting Information, SI). All ligands chosen for this study interact with Fe through carboxyl groups, however the number of potentially free (i.e., non-Fe complexed) carboxyl groups differs between the ligands. PGA ($(C_6H_8O_6)_n$, MW = 25−50 kDa, pK_a = 3.48 (25 °C)) consists of linear chains of partially methylated (1−4) linked α-D-galacturonic acid monomers. Previously, PGA has been used to model the acidic carbohydrate-rich OM fraction found in *Gola di Lago* freshwater flocs,[27] and has been shown to hinder Fe(II)-catalyzed secondary mineral formation in ferrihydrite-PGA coprecipitates.[8,9] In this study, PGA represents a HMW organic acid likely containing an excess of carboxyl groups in the ferrihydrite-PGA coprecipitate, resulting in negatively charged particles at circumneutral pH.[5] In contrast, GA ($C_6H_9O_7$, MW = 194 Da, pK_a = 3.48 (25 °C)) is the monosaccharide equivalent of PGA, representing a LMW organic ligand with zero free carboxyl groups in the coprecipitate. Because PGA and GA share similar chemical structures (Figure S1), a second LMW organic ligand with different chemical properties was additionally included to test the impact of MW versus chemical structure. Citric acid ($C_6H_5O_7$, MW = 192 Da, p$K_{a1,2,3}$ = 3.13, 4.76, 6.4 (25 °C)) is an α-hydroxy acid containing three carboxyl groups and is commonly found in nature. While complexation of Fe(II) with citrate-like groups may inhibit Fe(II) oxidation,[28] ferrihydrite precipitated in the presence of citric acid was shown to have smaller particle size compared to pure ferrihydrite.[21] With additional carboxyl groups, ferrihydrite-CA coprecipitates also comprise an LMW organic acid that may additionally influence atom exchange kinetics and mineral transformations via changes in surface charge of the coprecipitate.

DOI: 10.1021/acs.est.9b03952
Environ. Sci. Technol. 2019, 53, 13636−13647

Coprecipitate Synthesis. All solutions used in this experiment were prepared from doubly deionized (DDI) water (Milli-Q, Millipore, 18.2 MΩ·cm). The synthesis of 2-line ferrihydrite (Fh) and the ferrihydrite-OM coprecipitates followed methods previously described.[5,8,29] Briefly, ferrihydrite was prepared by adding 1 M NaOH (Titrisol) to 500 mL of a 200 mM Fe(III) solution ($Fe(NO_3)_3{\cdot}9H_2O$, Merck) under vigorous stirring (1200/min) until a pH of 7.0 ± 0.1 was obtained. For the ferrihydrite-OM coprecipitates, an ideal C:Fe molar ratio of 0.7 was chosen to minimize aqueous Fe(III) complexation by OM; a potential product during ferrihydrite coprecipitation with citrate at higher C:Fe molar ratios.[21] Furthermore, previous work with ferrihydrite-PGA coprecipitates indicated that below a C:Fe molar ratio of 1.2, surface-associated or organically complexed Fe(II) formed during reactions with Fe(II) is not expected to be above detection limits of spectroscopic methods,[9] therefore differences in mineral transformation products or kinetics in this study are likely not attributed to preferential complexation of Fe(II) by organic functional groups. To obtain similar C:Fe molar ratios in the ferrihydrite-OM coprecipitates, between 150 and 250 mg of PGA (≥90% (enzym.), Sigma-Aldrich), CA (≥98%, Sigma-Aldrich), or GA (≥98%, Sigma-Aldrich) was equilibrated overnight in darkness in 1 L DDI water adjusted to pH 7.0 with 1 M NaOH under vigorous stirring (1200/min). The ligand-containing solutions were then acidified to pH 4.0 with 1 M HNO_3 (Titrisol) and purged with $N_2(g)$ for 15 min. Afterward, 50 mL of a 200 mM Fe(III) solution ($Fe(NO_3)_3{\cdot}9H_2O$, Merck) were added, followed by the addition of 1 M NaOH as described in the synthesis of ferrihydrite. The ferrihydrite and ferrihydrite-OM (co)precipitates were then repeatedly centrifuged at 3500g for 15 min, decanted, and resuspended in 700 mL DDI water until the electric conductivity of the supernatants was ≤100 μS/cm. Afterward, the suspensions were shock-frozen by dropwise injection into liquid N_2,[30] freeze-dried, manually homogenized with a mortar and pestle, and stored in brown glass in a desiccator until use. The synthetic ferrihydrite-OM coprecipitates are hereafter named Fh-PGA, Fh-CA, and Fh-GA.

(Co)precipitate Characterization. Total C contents of (co)precipitates were analyzed with an elemental analyzer (CHNS-932, LECO; $n = 2$). For total Fe determination, ~2 mg of (co)precipitate material were dissolved in 1 mL of 30% HCl (Ultrapur, Merck), diluted with 1% HCl to 30 mL, and measured with atomic absorption spectrometry (AAS, Varian AA240FS). The electrophoretic mobility of the (co)precipitates was measured with a ZetaPALS Zeta Potential Analyzer (532 nm laser, Brookhaven Instr. Corp.). For these measurements, 250 mg/L (co)precipitate was resuspended in 10 mM NaCl (EMSURE, Merck). The solution was vigorously stirred (1200/min) and continually degassed by purging with $N_2(g)$, while the pH was adjusted with dilute HCl or NaOH. Once the desired pH was obtained and remained constant for 10 mintutes, 20 mL aliquots of the solution were removed and ultrasonicated for 5 min. Directly afterward, the average electrophoretic mobility was determined from 10 runs comprising 10 cycles each. The measurements were repeated in duplicates, and the accuracy of the electrophoretic mobility measurement was checked against the BI-ZR3 zeta potential reference material (Brookhaven Instr. Corp.). The mineral surface areas of the (co)precipitates were determined by 11-point N_2−BET measurements (Quantachrome, Autosorb-1 MP) after 48 h of outgassing at 30 °C. Specific surface areas (SSA) were estimated after correcting for an assumed negligible N_2 gas adsorption onto the OM:[5,31]

$$\mathrm{SSA}^{\mathrm{corr}} = SSA/(1 - (f\mathrm{OC}_{\mathrm{L}} \times \mathrm{OC})/1000) \quad (1)$$

where SSA is the measured specific surface area (m^2/g), $f\mathrm{OC}_\mathrm{L}$ is the fraction of C in the ligand ((−), Table S1) and OC is the C content of the sample material (mg/g, Table S2). However, SSA measurements are to be considered with caution; particle aggregation may be impacted by flash-freezing and freeze-drying,[5,30] and gas adsorption onto dry materials may not be representative of available surface areas after particle disaggregation upon resuspension.

Quantitative mineral-phase analyses were performed by powder X-ray diffraction (XRD, D8 Advance, Bruker) with Rietveld analysis. Dried sample material (~2 mg) was resuspended in ethanol (~30 μL, Merck) and pipetted onto a polished silicon wafer (Sil'tronix Silicon Technologies, France). Samples were analyzed in Bragg−Brentano geometry using Cu Kα radiation (λ = 1.5418 Å, 40 kV, and 40 mA) and a high-resolution energy-dispersive 1-D detector (LYNXEYE). Diffractograms were recorded from 10° to 70°2θ with a step size of 0.02°2θ and 10 s acquisition time per step. The relative contributions of mineral phases in diffraction patterns was determined by Rietveld Quantitative Phase Analysis (QPA) with 2-line ferrihydrite included as mass-calibrated PONKCS (Partial Or No Known Crystal Structure)[32] phase. All calculations were performed in TOPAS software (Version 5, Bruker AXS) where, in addition to ferrihydrite, only crystalline phases which could be identified by the presence of a characteristic diffraction peak were accepted for the final fits. The validity of this method has previously been shown for mixtures with known mass ratios, whereby the contribution of ferrihydrite can be well quantified in mixtures with crystalline mineral phases so long as it is a major component.[8,33] Unreacted coprecipitates were additionally imaged with electron microscopy (EM). For these analyses, ~2 mg of solid-phase material was resuspended in 10 μL of DDI water and drop-deposited onto a 200 mesh Cu grid coated with a holey C-coated support film (SPI supplies). Microscopy images were obtained with a dedicated scanning transmission electron microscope (STEM, 2700Cs, Hitachi) operated at an acceleration voltage of 200 kV. A secondary electron (SE) or high angular annular dark field (HAADF) detector was used for image acquisition.

^{57}Fe(II) Isotope Tracer Experiments. The experimental setup was similar to previous enriched stable isotope tracer studies, where ^{57}Fe(II) was used as a stable isotope tracer to explore atom exchange during Fe(II)-catalyzed mineral transformations.[8,9] Briefly, triplicate experiments were conducted in a glovebox (N_2 atmosphere, <1 ppm (v/v) O_2), where all glassware and solutions were equilibrated for >2 days to remove trace O_2. A ^{57}Fe-enriched stock solution of 1 M Fe(II) was prepared by dissolving ^{57}Fe metal powder (95.08% ^{57}Fe, Isoflex, U.S.A.) in 2 M HCl at 70 °C overnight, which was then purged with $N_2(g)$, sealed, transferred into the glovebox, and diluted with anoxic DDI water to obtain a 100 mM ^{57}Fe(II) solution in 0.2 M HCl. The Fe concentration of the ^{57}Fe(II) solution was determined in 0.22-μm nylon filtrates with AAS. ^{57}Iron(II)$_{\mathrm{spike}}$ reactions were conducted in 50 mL glass serum bottles wrapped in Al foil to prevent photochemical reduction of Fe(III) to Fe(II) by the CA. Dried sample material was weighed into each bottle and equilibrated for 16 h in ~45 mL of anoxic 50 mM 3-(*N*-morpholino)-propanesulfonic acid (MOPS) buffer adjusted to pH 7. Solid to solution ratios ranged from 1.01 to 1.45 g/L in order to obtain equivalent solid-phase Fe concentrations in each bottle (10 mM Fe(III), Table S3). Reactions were started when aliquots of the 0.22-μm filtered ^{57}Fe(II) stock solution were added to the bottles, obtaining final Fe(II)$_{\text{spike}}$ concentrations of 1.0 mM (Table S3). No additional pH adjustments were required, and pH remained at 7.0 ± 0.1 for the duration of the experiment. Serum bottles were capped with butyl rubber stoppers and set on an orbital shaker (250 rpm) at room temperature (24 ± 1 °C) for 1 week. Iron(II)-free controls were included for each treatment to quantify element releases originating from solid-phase dissolution.

Total Fe$_{\text{aq}}$ Concentrations and Fe Isotope Measurements. Total aqueous Fe (Fe$_{\text{aq}}$) concentrations were determined in 0.22-μm nylon filtrates via AAS while Fe$_{\text{aq}}$ speciation at 1 week was determined with the 1,10-phenanthroline method[34] (λ = 510 nm, Cary 60 UV–vis, Agilent). Iron isotope compositions were determined via inductively coupled plasma-mass spectrometry (ICP-MS, Agilent 8800 Triple Quad). All samples for isotope analysis were diluted to ~50 μg Fe/L and measured in reaction cell mode with an $H_2(g)$ flow rate of 7 mL/min to remove argide polyatomic interferences. Iron isotope mole fractions (f) were calculated by dividing the counts per second (cps) of the Fe isotope n by the sum of the total Fe isotope's cps:

$$\frac{^{n}\text{Fe}_{cps}}{^{54}\text{Fe}_{cps} + {}^{56}\text{Fe}_{cps} + {}^{57}\text{Fe}_{cps} + {}^{58}\text{Fe}_{cps}} \times 100 = f^{n}\text{Fe}(\%) \tag{2}$$

The accuracy of this method has been previously established[8,9] and was tested with the Fe isotopic reference material IRMM-014.[35]

The use of stable Fe isotopes enables the investigation of iron atom exchange between Fe(III) minerals and Fe$_{\text{aq}}$. In this study, synthetic (co)precipitates containing natural Fe isotope abundances (f^{54}Fe: ~5.85%, f^{56}Fe: ~91.75%, f^{57}Fe: ~2.12%, f^{58}Fe: ~0.28%),[9,35] were reacted with a highly ^{57}Fe enriched Fe(II) solution (f^{54}Fe: 0.05%, f^{56}Fe: 3.01%, f^{57}Fe: 95.08%, f^{58}Fe: 1.86%). Because the Fe(II)$_{\text{spike}}$ consisted primarily of ^{57}Fe (95.08%), Fe isotope composition is discussed in terms of f^{57}Fe. Calculation of the isotopic composition of the total system is presented in Table S4.

Fe(II)-Reacted Solid-Phase Sampling and Characterization. Material for solid-phase analyses was collected on 0.45-μm cellulose filters and thoroughly rinsed with anoxic DDI water. The filter residues were covered and dried in the glovebox atmosphere. Triplicate samples were combined, homogenized with a mortar and pestle, and stored in the dark until further analyses. Total C and Fe contents, Fe isotope composition, and QPA of XRD patterns of Fe(II)-reacted (co)precipitates were determined via the methods described above. Iron(II)-reacted samples were additionally imaged with EM as described above. For these analyses, grids were prepared under anoxic conditions, then transported to the microscope and imaged within 3 h.

X-ray Absorption Spectroscopy. Speciation of solid-phase Fe in the coprecipitates before and after reaction with Fe(II) were analyzed by bulk Fe K-edge (7112 eV) X-ray absorption spectroscopy (XAS) at the XAFS beamline of ELETTRA (Trieste, Italy). For these analyses, (un)reacted (co)precipitate material was pressed into 1.3 cm pellets and sealed with Kapton tape. Iron(II)-reacted samples were prepared and transferred to the beamline under anoxic conditions. X-ray absorption near edge structure (XANES) and extended X-ray absorption fine structure (EXAFS) spectra were recorded in transmission mode at ~80 K using a $N_2(l)$ cryostat and a Si(111) monochromator calibrated to the first-derivative maximum of the K-edge absorption spectrum of a metallic Fe foil (7112 eV). The foil was continuously monitored to account for small energy shifts (<1 eV) during the sample measurements. Higher harmonics in the beam were eliminated by detuning the monochromator by 30% of its maximal intensity. Three scans per sample were collected and averaged. All spectra were energy calibrated, pre-edge subtracted, and postedge normalized in Athena,[36] and the edge-energy (E_0), was defined as the zero-crossing in the second XANES derivative. Linear combination fit (LCF) analyses of k^3-weighted Fe K-edge EXAFS spectra were performed over a k-range of 2–12 Å^{-1} with the E_0 of all spectra and reference compounds set to 7128 eV. No constraints were imposed during LCF analyses, and initial fit fractions were recalculated to a compound sum of 100%. It should be noted, that reference spectra for Fe(III)-citrate, Fe(III)-EDTA, Fe(III)-oxalate hexahydrate, Fe(II)-D-gluconate dehydrate, and Fe(II)-oxalate dehydrate were offered in the fits, however organically complexed Fe(II) or Fe(III) was not detected in any of our samples. Shell-fit analyses of k^3-weighted Fe EXAFS spectra of (un)reacted Fh-OM coprecipitates were performed in R-space (R-range = 1.0–3.5 Å, k-weight = 3, k-range 2–12 Å) using Artemis.[36] Theoretical phase-shift and amplitude functions were calculated with FEFF v.6[37] based on the structures of goethite[38] (α-FeOOH) and lepidocrocite[39] (γ-FeOOH). The passive amplitude reduction factor, S_0^2, was determined from a multispectrum fit of the first O shell of all samples (n = 5, R-range = 1.0–2.1 Å, k-weight = 3, k-range 2–12 Å). The fitted value of 0.77 corresponds well to previously published data[5,20,21] and was later fixed in all individual fits.

RESULTS AND DISCUSSION

Coprecipitate Characterization. Total C and Fe contents of the ferrihydrite-OM coprecipitates ranged from 53 to 62 (C) and 471 to 524 (Fe) mg/g, resulting in similar C:Fe molar ratios of 0.60, 0.52, and 0.54 for Fh-PGA, Fh-CA, and Fh-GA, respectively (Table S2). The estimated point of zero charge (PZC) for the pure ferrihydrite was 8.2 (Figure S2), indicating that ferrihydrite has a slightly positive surface charge at pH 7. Carboxyl functional moieties of the organic ligands interact with the hydroxyl groups of the precipitating ferrihydrite via ligand exchange,[6,40] therefore Fh-GA, which contains only 1 carboxyl group, should retain a surface charge similar to that of the OM-free ferrihydrite, as coprecipitation with GA leaves no residual free carboxyl groups. In contrast, both Fh-PGA and Fh-CA likely contain an excess of carboxyl groups, resulting in a negative surface charge at pH 7 (Figure S1). In agreement with this expected increase in non-complexed carboxyl groups, the estimated PZC for the OM-containing coprecipitates progressively decreased (Fh-GA$_{\text{pzc}}$ > Fh-CA$_{\text{pzc}}$ > Fh-PGA$_{\text{pzc}}$, Figure S2). Specific surface area measured for the dried OM-free ferrihydrite was 296 m^2/g (Table S2), in agreement with literature values for dried 2-line ferrihydrite (~300 m^2/g).[29] In comparison, all coprecipitates exhibited reduced estimated SSA compared to the pure

Table 1. Linear Combination Fit Results for Fe K-Edge EXAFS Spectra Prior to and after 1 Week Reaction with 1 mM Fe(II)

sample		Fh (%)	Lp (%)	Mgt (%)	NSSR[a] (%)	red. χ^{2b} (−)
Fh	initial[c]	100			1.6	0.080
	+ 1 mM Fe(II)		82	18	2.4	0.014
Fh-PGA	initial	100			1.1	0.002
	+ 1 mM Fe(II)		94	6	1.1	0.005
Fh-CA	initial	100			1.3	0.003
	+ 1 mM Fe(II)	81	19		1.3	0.003
Fh-GA	initial	100			1.7	0.004
	+ 1 mM Fe(II)	100			1.3	0.003

[a]NSSR: Normalized sum of squared residuals ($100 \times \sum_i(\text{data}_i\text{-fit}_i)^2/\sum_i \text{data}^2$). [b]Fit accuracy (reduced $\chi^2 = (N_{idp}/N_{pts})\sum_i((\text{data}_i - \text{fit}_i)/\varepsilon_i)^2(N_{idp} - N_{var.})^{-1}$. N_{idp}, N_{pts}, and $N_{var.}$ are, respectively, the number of independent points in the model fit (16), the total number of data points (201), and the number of fit variables (1−2). ε_i is the uncertainty of the i^{th} data point.[76] [c]Samples were measured for a previous publication.[9] Abbreviations: Fh = ferrihydrite, PGA = polygalacturonic acid, CA = citric acid, GA = galacturonic acid.

ferrihydrite (Table S2). Coprecipitation with a HMW versus LMW ligand may potentially impact aggregate structure, whereby large molecules could bridge between ferrihydrite particles to form aggregates with polymeric organic matter enclosed, while small molecules may coat the surface but not bridge to other particles. However, EM imaging of the unreacted (co)precipitates revealed that all materials, including the OM-free ferrihydrite, consisted of dense aggregates ≥1 μm in size (Figure S9). This, combined with the SSA results, suggests that OM was preferentially distributed on the surface of the dried coprecipitates, thereby reducing overall N_2 sorption.

LCF analysis of Fe K-edge EXAFS spectra of the unreacted (co)precipitates (Figure S3) highlighted the similarities between the unreacted solid materials, with each being satisfactorily fit by only ferrihydrite (Table 1). The absence of organically complexed Fe(III) is expected considering the low C:Fe molar ratios of the coprecipitates used in this study.[8,21] In order to ascertain whether coprecipitation with the various organic ligands influenced the local Fe coordination, shell-fit analyses were performed on Fourier-transformed Fe K-edge EXAFS spectra of unreacted (co)precipitates. All spectra were dominated by two features in R-space (Figure 1), the first of which was satisfactorily fit for all samples by a single Fe−O shell at ca. 1.97 Å (Table 2).[5,21] First shell amplitudes and fitted coordination numbers (CN) and Debye−Waller parameters (σ^2) were similar for all (co)precipitates (Figure S4 and Table 2, respectively), confirming structural similarities and minimal differences in distortion of first shell neighbors in all the (co)precipitates. In contrast, the second feature, visible at ∼2.8 Å ($R + \Delta R$), indicated subtle differences in the ferrihydrite (co)precipitates (Figure 1). All samples were consistently fit with two Fe−Fe scattering paths at distances of 3.05 and 3.43 Å; corresponding to edge- and corner-sharing Fe (Fe−Fe_1 and Fe−Fe_2, respectively). To reduce the number of fit parameters in final fits, the σ^2 parameters of the Fe shells were set to 0.013 (Fe−Fe_1) and 0.011 (Fe−Fe_2). These values were determined as the average σ^2 applied for edge- and corner-sharing Fe in ferrihydrite-polygalacturonic acid[5] and ferrihydrite-citric acid[21] coprecipitates, and are within the range of published σ^2 values for ferrihydrite and other ferrihydrite-OM coprecipitates.[20,41−44] Multiple scattering (MS) within the Fe(O,OH)_6 octahedron was also accounted for with the inclusion of a constrained MS path.[20,27] As expected,[5,21,45] coprecipitation with the organic ligands used in this study did not influence Fe−Fe distances in the ferrihydrite structure. However, reduced amplitudes in the second feature of all OM-containing samples (Figure S4) corresponded to decreases in fitted CN of up to 10% (Fe−Fe_1) and 42% (Fe−Fe_2) relative to the OM-free ferrihydrite (Table 2). This may indicate overall smaller ferrihydrite particle size in the coprecipitates,[21,45] suggesting that coprecipitation with organic ligands impeded ferrihydrite crystal growth, at which the lower molecular weight organic ligands (CA and GA) were most effective. In addition, CN for the Fe shells revealed smaller ratios between corner- and edge-sharing Fe in the coprecipitates compared to the OM-free ferrihydrite, with the lowest ratio found in Fh-CA (Table 2). This is consistent with the surface depletion model,[46] whereby, with decreasing particle size, contributions from unstable octahedral and tetrahedral Fe (corner-sharing) are depleted in favor of stable octahedral Fe (edge-sharing).[47] Alternatively, reduced CN specific to corner-sharing Fe suggests inhibited crystal growth

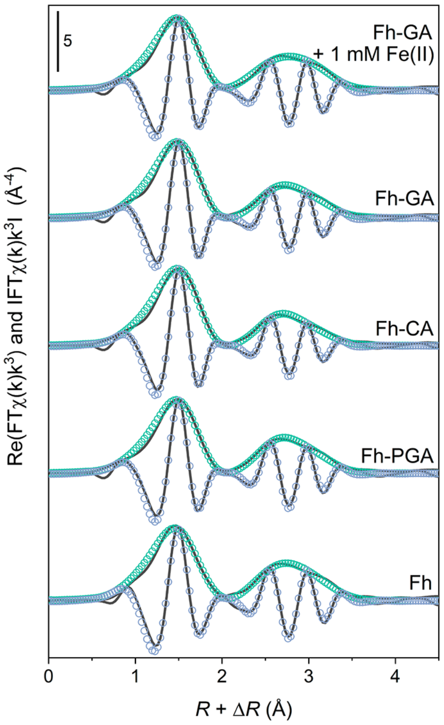

Figure 1. Iron K-edge Fourier-transform magnitudes and real parts of unreacted (co)precipitates and Fh-GA reacted with 1 mM Fe(II) for 1 week. Solid lines indicate experimental data and open circles show the model fits. Shell-fit parameters are reported in Table 2.

Table 2. Shell-Fit Parameters Determined from Fe K-Edge EXAFS Spectra of (Un)reacted (Co)precipitates[a]

	Fe−O			$Fe-Fe_1$		$Fe-Fe_2$					
sample	CN[b]	R(Å)[c]	σ^2[d]	CN	R(Å)	CN	R(Å)	CN[e] ratio	ΔE_0[f] (eV)	NSSR[g] (%)	red. χ^2[h]
Fh	6.3 (9)	1.96 (1)	0.011	2.9 (5)	3.04 (2)	3.1 (6)	3.43 (2)	1.05	−4.9 (1.5)	1.0	407
Fh-PGA	5.6 (4)	1.97 (1)	0.010	3.0 (3)	3.05 (1)	2.3 (3)	3.44 (1)	0.75	−3.7 (9)	0.5	1558
Fh-CA	5.7 (4)	1.98 (1)	0.009	2.8 (3)	3.06 (1)	1.8 (3)	3.43 (2)	0.64	−3.4 (8)	0.5	1744
Fh-GA	5.9 (4)	1.97 (1)	0.009	2.7 (3)	3.05 (1)	2.2 (4)	3.44 (1)	0.81	−3.4 (9)	0.6	1207
Fh-GA+ 1 mM Fe(II)	5.8 (4)	1.98 (1)	0.011	2.9 (3)	3.05 (1)	2.6 (4)	3.44 (1)	0.92	−3.5 (9)	0.6	2194

[a] The passive amplitude reduction factor, S_0^2, was set to 0.77 based on a multispectrum fit of the first O shell for all samples ($n = 5$). Parameter uncertainties are shown for the last significant figure. The Debye−Waller parameters, σ^2, were fixed to 0.013 Å^2 ($Fe-Fe_1$) and 0.011 Å^2 ($Fe-Fe_2$). [b] Path degeneracy (coordination number). [c] Mean half path length. [d] Debye−Waller parameter. [e] CN_{Fe-Fe2}/CN_{Fe-Fe1}. [f] Energy-shift parameter. [g] Normalized sum of squared residuals ($100 \times \sum_i(\text{data}_i\text{-fit}_i)^2/\sum_i \text{data}^2$). [h] Fit accuracy; reduced $\chi^2 = (N_{idp}/N_{pts})\sum_i(\text{data}_i\text{-fit}_i)/\varepsilon_i)^2(N_{idp}\text{-}N_{var.})^{-1}$. N_{idp}, N_{pts}, and $N_{var.}$ are, respectively, the number of independent points in the model fit (16), the total number of data points (201), and the number of fit variables (8). ε_i is the uncertainty of the i^{th} data point. Note: Models also included a triangular Fe−O−O multiple scattering path constrained as follows: $N = 4CN_{Fe-O}$, $R = R_{Fe-O}(1 + \sqrt{2}/2)$, and $\sigma^2 = 2\sigma^2{}_{Fe-O}$.[20,27]

in the crystallographic z-axis,[48] thus resulting in more two-dimensional crystal morphology.

Rietveld QPA of XRD patterns of the unreacted (co)-precipitates confirmed the presence of 2-line ferrihydrite, visible as broad maxima around 2.54 and 1.49 Å (Figure S5). In general, characterization of the unreacted (co)precipitates showed that, in terms of structural disorder and aggregate morphology, all (co)precipitates were similar, however in terms of particle size, Fh-PGA was most similar to the pure ferrihydrite, while Fh-CA and Fh-GA tended to show reduced particle size and/or inhibited particle growth morphology.

Total Fe_{aq} Concentrations and Iron Isotope Measurements. Total dissolved Fe (Fe_{aq}) concentrations are shown in Figure 2 (left panels) with the corresponding Fe_{aq} isotope composition displayed in terms of the fraction of ^{57}Fe ($f^{57}Fe$) and the sum of the combined fractions of the remaining stable Fe isotopes; ^{54}Fe, ^{56}Fe, and ^{58}Fe ($f^{54+56+58}Fe$). These data are further summarized in Table S5. Analyses of dissolved Fe species at 1 week (data not shown) revealed that Fe(II) accounted for 98 ± 1% of total aqueous Fe in Fh-PGA and Fh-GA, in agreement with previous studies.[8] In Fh-CA, Fe(II) comprised 76 ± 11% of the total aqueous Fe, indicating that some Fe(III), likely organically complexed, may have persisted in solution. Because these contributions are minimal, discussions of Fe_{aq} in this paper refers to Fe(II). Estimated SSA of the coprecipitates, which suggested that the pure ferrihydrite and Fh-CA possessed the highest and lowest surface areas available for sorption (Table S2), proved to be poor indicators for Fe(II) adsorption trends. Rather, trends in Fe(II) adsorption within the first 6 h appear consistent with expected changes to the particle surface charge due to the presence of free carboxyl groups. Specifically, Fh-CA and Fh-PGA, both containing an excess of negatively charged carboxyl groups, recorded the lowest Fe_{aq} concentrations, accounting for the removal of ~66% of the initial Fe(II) spike. In contrast, Fe_{aq} concentrations were high in the excess carboxyl-free pure Fh and Fh-GA, where 52% and 54% of initial Fe(II) concentrations remained in solution. Our previous work with ferrihydrite-PGA coprecipitates showed that Fe(II) complexation by PGA-carboxyl groups alone could not account for differences in rapid (<6 h) Fe(II) adsorption trends.[8] As the coprecipitates in the current study comprise lower C:Fe molar ratios (C:Fe = 0−2.5 in ref 8 vs C:Fe ≈ 0.5, Table S3), we assume here that Fe(II) adsorption trends are similarly dominated by Fe(II)-mineral interactions. For the OM-free Fh, magnetite accumulation after 6 h coincided with the removal of nearly all Fe(II) from solution (Figure 1A). For all OM-containing samples, in the absence of notable magnetite precipitation, Fe_{aq} concentrations remained relatively stable. It should be noted that at the low coprecipitate C:Fe molar ratios applied in this study (Table S2), complexation of Fe(II) by the organic fraction and/or the formation of surface-associated Fe(II) is not expected to be above detections limits for Mössbauer or synchrotron methods (<5 mol %),[8,9] and therefore all Fe(II) in the system is assumed to be available to participate in Fe(II)-catalyzed atom exchange and mineral transformation processes.

In a similar study involving Fe(II)-reacted ferrihydrite-humic and -fulvic acid coprecipitates, Zhou et al.[12] concluded that the amount of Fe(II) that sorbed could not account for differences in the Fe(II)-catalyzed mineral transformation products. Our findings support their argument in that, despite the nearly identical extent of Fe(II) adsorption observed at 6 h for the pure ferrihydrite and Fh-GA, and Fh-PGA and Fh-CA, respectively, both the mineral transformation kinetics (Figure 2 as well as rates of iron atom exchange (Figure S6) varied significantly between these samples. Of all the (co)precipitates, significant inhibition of atom exchange was recorded only in Fh-GA (Figure S6). With a PZC near pH 5.4 (Figure S2) and assuming a slightly positive surface charge similar to that of the OM-free ferrihydrite, it is possible that diffusion of Fe(II) through Fh-GA was slower compared the Fh-PGA and Fh-CA; whose excess of carboxyl groups and lower PZC indicated negatively charged functional groups in the aggregate core. For the other samples, in agreement with previous work,[8] minimum fractions of ^{57}Fe in solution ($f^{57}Fe_{aq}$) exceeded the calculated isotope composition of the entire system within the first 48 h in some samples (Figure S6, Table S4). For the OM-free Fh, the maintenance of low $f^{57}Fe_{aq}$ may be explained through the incorporation of nearly all Fe(II) during magnetite accumulation after 6 h (Figure 2A) while for the coprecipitates, low $f^{57}Fe_{aq}$ may indicate the formation of a ^{57}Fe-enriched crystalline solid-phase like lepidocrocite or goethite,[8] both of which would undergo continued atom exchange, albeit at significantly slower rates than ferrihydrite.[22]

Solid-Phase Analyses: XRD and XAS. The consequences of continued iron atom exchange are apparent in the right two panels of Figure 2, where X-ray diffraction patterns and their corresponding QPA fits illustrate the temporal evolution of solid-phase mineral transformations in Fe(II)-reacted (co)-precipitates. In agreement with previous studies,[8−12] formation of secondary crystalline mineral phases occurred to a lesser

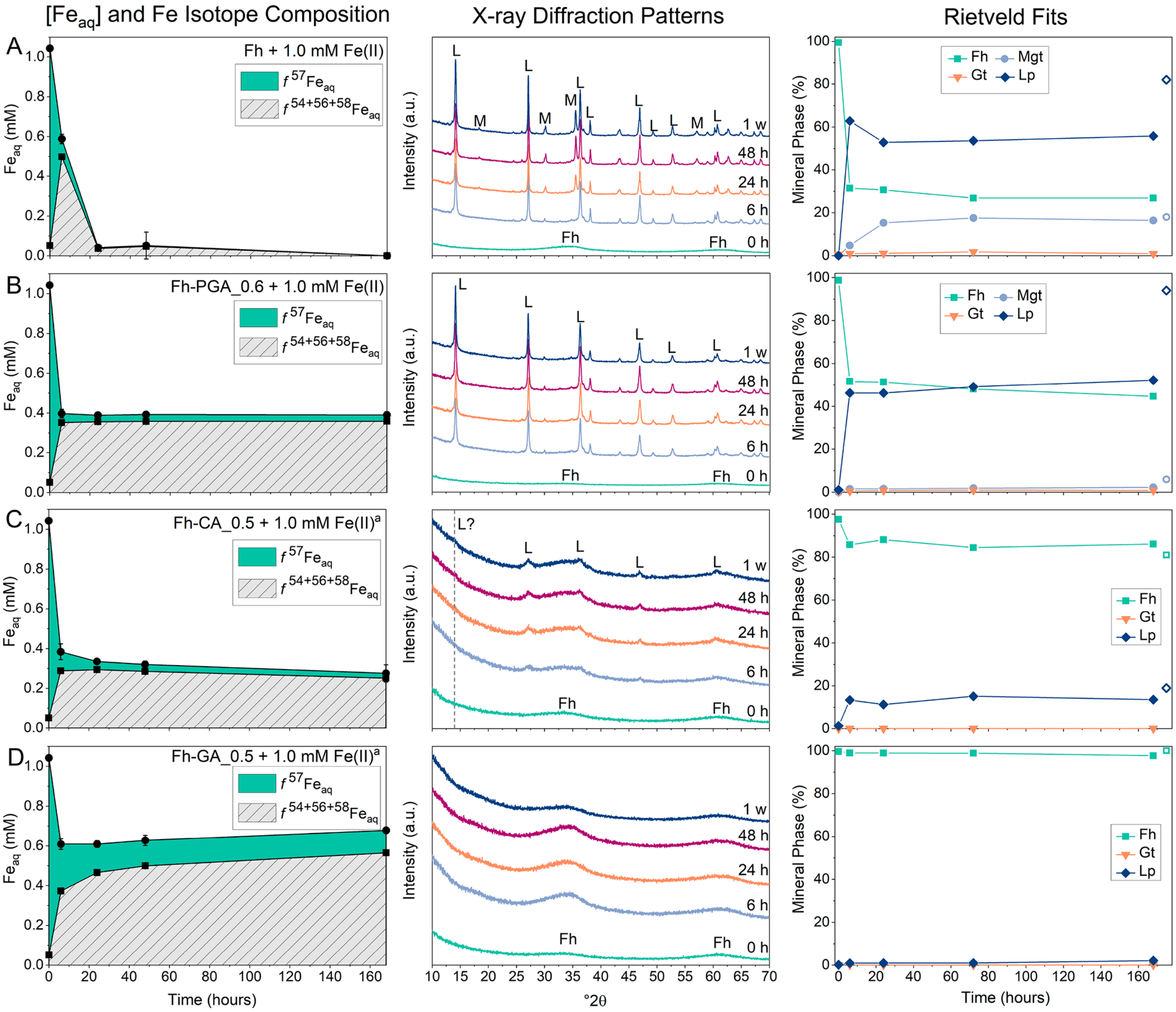

Figure 2. (Left panels) Dissolved Fe (Fe$_{aq}$) concentrations and iron isotope composition of Fe$_{aq}$ shown in terms of the fraction of ^{57}Fe (f^{57}Fe) and the combined fractions of ^{54}Fe, ^{56}Fe, and ^{58}Fe ($f^{54+56+58}$Fe). Lower and upper error bars indicate the standard deviation in Fe isotope composition and of total dissolved Fe from triplicate reactors, respectively. (Middle panels) X-ray diffraction patterns of samples prior to and during reactions with 1.0 mM Fe(II) and (Right panels) corresponding mineral phase contributions determined with Rietveld QPA. The open symbols to the right indicate results from linear combination fit analysis of Fe K-edge EXAFS spectra of 1 week Fe(II)-reacted (co)precipitates (Table 1). Abbreviations: h = hours, w = week, Fh = ferrihydrite, Gt = goethite, L/Lp = lepidocrocite, Mgt = magnetite, PGA = polygalacturonic acid, CA = citric acid, GA = galacturonic acid. ^{a}Samples contained ≤1% siderite (contribution not shown in Rietveld fit).

extent in the OM-containing coprecipitates. Magnetite contributed to 16% of Fe mineral phases in the OM-free Fh at 1 week, in contrast to ≤3% in the coprecipitates (Table S6). Lepidocrocite accounted for the remainder of crystalline mineral phases detected (2−56%, Table S6). In comparison to the narrow peaks assigned to lepidocrocite in the OM-free Fh and Fh-PGA, lepidocrocite peaks in Fh-CA appeared broadened (Figure 2), suggesting generally smaller lepidocrocite crystallite sizes in the Fe(II)-reacted Fh-CA. Indeed, fitted lepidocrocite crystallite sizes in Fe(II)-reacted Fh, Fh-PGA, and Fh-CA at 1 week decreased from 39 to 29 to 13 nm, respectively (LVol-IB, determined with Double-Voigt Approach fitting Cry size L during QPA in TOPAS). Unique to the Fe(II)-reacted Fh-CA lepidocrocite, of notable absence is the typically dominant (020) reflection (d = 6.2895 Å, ca. 14°2θ, Figure 2C), indicating extremely thin lepidocrocites. A similar absence of the (020) reflection has been recorded for nanolepidocrocite found in organic-rich, freshwater flocs.[27] Because freshwater flocs also contain carboxyl-rich organic groups[27] and a consortia of coexisting Fe(III)-reducing and Fe(II)-oxidizing bacteria,[49] it is plausible that floc nanolepidocrocite may form via similar Fe(II)-catalyzed reactions impacted by citrate-like OM. No secondary crystalline minerals were detected with XRD in Fe(II)-reacted Fh-GA.

Because XRD methods are not sensitive to organically complexed or adsorbed Fe(II/III), and may not discriminate nanometer-sized clusters of lepidocrocite or goethite from ferrihydrite,[8] the composition of Fe minerals determined via XRD may differ from other solid-phase analysis techniques, such as XAS or Mössbauer spectroscopy.[8,9,27] Therefore, we

DOI: 10.1021/acs.est.9b03952
Environ. Sci. Technol. 2019, 53, 13636−13647

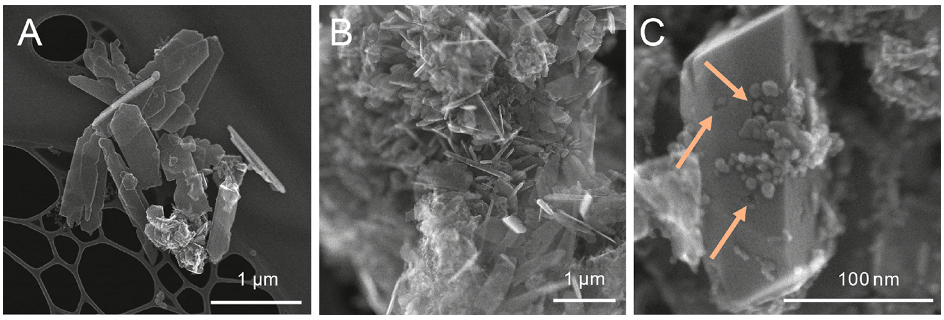

Figure 3. Secondary electron (SE) images of the pure ferrihydrite reacted with 1 mM Fe(II) at 1 week. (A) Lath-like lepidocrocites. (B) Lath-like lepidocrocites embedded in an aggregate with residual ferrihydrite. (C) Aggregate containing (nano)magnetite and ferrihydrite. Arrows point to surface holes in the magnetite crystal which appear to be filled in by nanomagnetite clusters.

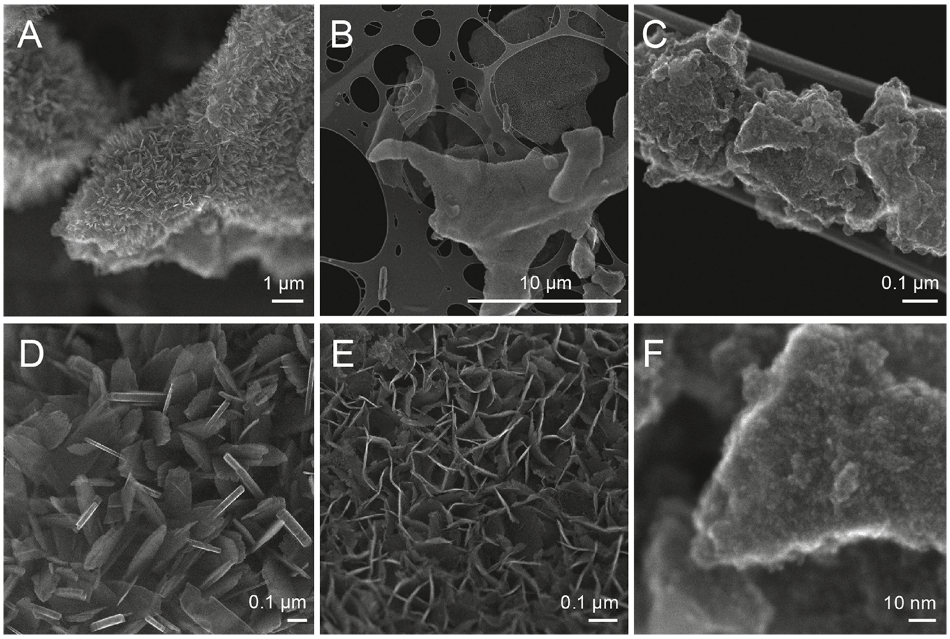

Figure 4. Secondary electron (SE) images of Fe(II)-reacted (A,D) Fh-PGA and (B,E) Fh-CA show "hedge-hog-like"[60] growth of laminar lepidocrocites around an aggregate structure. No crystalline mineral phases were identified in Fh-GA (C,F). Lepidocrocites in (D) Fh-PGA were 20−60 nm thick ((001) reflection), whereas Fh-CA lepidocrocites (E) were <10 nm thick (001) and the (020) face reflection is visibly crumpled.

additionally employed synchrotron techniques and EM to supplement information regarding (co)precipitate Fe mineralogy after reaction with Fe(II). Results from LCF analysis of Fe K-edge EXAFS spectra of Fe(II)-reacted (co)precipitates are indicated as symbols in the far right panel of Figure 2 to facilitate comparison between XRD and XAS data at the end of the experiment. Spectra and model fits are independently shown in Figure S8, and LCF results are detailed in Table 1. For Fh-CA and Fh-GA, results from LCF analysis are in very good agreement with Rietveld QPA ($\Delta \leq 4\%$, Figure 2, right panel). In contrast, for both the OM-free Fh and Fh-PGA, LCF recorded significantly less ferrihydrite ($\Delta \leq 45\%$, Figure 2, right panel), instead reporting lepidocrocite as the dominant secondary mineral phase. Because EXAFS detects local coordination environments (<4 Å), it is possible that LCF reported a mixture of crystalline and nanolepidocrocite, the latter of which would be difficult to distinguish from other amorphous phases (e.g., ferrihydrite) in XRD patterns, thus leading to an overestimation of ferrihydrite-PONCKS phase. However, additional testing of the XRD QPA fits showed that the exclusion of ferrihydrite significantly reduced the fit quality (e.g., increased the Goodness of Fit (GOF) parameter, Figure S7). In addition, substantial ferrihydrite was also identified in EM images (Figures 3 and 4A, discussed below). Therefore, ferrihydrite was included as a mass-calibrated PONKCS phase for the final fits, although the contribution of nanolepidocrocite to the fitted fraction cannot be excluded.

Organic-rich ferrihydrite has been shown to partake in atom exchange without undergoing mineral transformations to crystalline phases.[8,9,12] For crystalline goethite, depending on the starting crystallite size, such Fe(II)-catalyzed recrystallization may result in anisotropic changes in crystal morphology without mineral transformation.[23,50−52] However, the extent to which Fe(II)-catalyzed iron atom exchange and recrystallization alters ferrihydrite morphology remains unclear.[12] Therefore, Fh-GA, which comprised only ferrihydrite after reaction with Fe(II) (≥98%, Figure 2D, Table 1), presents an ideal opportunity to examine if atom exchange resulted in structural or morphologic changes in the residual ferrihydrite. To this end, we also performed shell-fit analysis on Fe K-edge EXAFS spectra of the Fe(II)-reacted Fh-GA (Figure 1, Table 2). Slight increases in second shell amplitude in the Fe(II)-reacted Fh-GA (Figure S4) were accompanied by a higher fitted average CN for the Fe shells (Table 2), suggesting an increase in particle size.[21,33] While a general increase in particle size may indicate crystal growth via Ostwald ripening or oriented aggregation, the selective increase in corner-sharing (versus edge-sharing) Fe (+15% vs +7%) suggests that crystal growth primarily occurred in the same crystallographic plane, specifically the *z*-axis.[48] Collectively, these results suggest that ferrihydrite nanoparticles in the Fe(II)-reacted, recrystallized Fh-GA more resembled the pure ferrihydrite.

Electron Microscopy. A selection of secondary electron (SE) images presented in Figures 3 and 4 highlight variations in crystallinity, morphology, and distribution of (secondary) mineral phases found in the Fe(II)-reacted (co)precipitates. Additional images are provided in the SI. Corroborating XRD and XAS data, Fe(II)-reacted ferrihydrite was dominated by sheet-like lepidocrocites and aggregates in which (nano)-crystalline mineral phases and residual ferrihydrite were observed (Figure 3). Of note is Figure 3C, where open pits on the surface of a ca. 100 nm-sized magnetite appear to be filled by 5−12 nm-sized clusters. Ferrihydrite nanoparticles are cited to be on the order of ≤10 nm,[48,53,54] with freshly precipitated ferrihydrites presenting even smaller crystallite sizes (1−3 nm[54,55]). As evidenced in the larger particle size in the Fe(II)-reacted Fh-GA, interactions with Fe(II) may stimulate ferrihydrite nanoparticle growth. However, above 8 nm, ferrihydrite nanoparticles are thermodynamically unstable at room-temperature, spontaneously transforming to nano-goethite or -hematite.[56,57] Therefore, the larger nanoclusters of Figure 3C are likely nanomagnetite, while the surface holes on the large magnetites may be dissolution pits associated with the Fe(II)-catalyzed "redox-driven conveyer belt" model previously suggested for goethite,[51] hematite,[58] and magnetite.[59]

In contrast to the μm-sized, sheet-like lepidocrocites of the OM-free ferrihydrite, Fe(II)-reacted Fh-PGA and Fh-CA largely retained their unreacted bulk morphologies (Figure S9); both are characterized by large aggregates (1−10 μm) covered in nm-sized laminar lepidocrocites, also described as "hedge-hog-like"[60] or "bird's nest type"[61] (Figure 4A,B). Similar mineral morphologies have been imaged growing on organic stalks in the presence of microaerophilic Fe(II)-oxidizing bacteria,[18,62] where carboxyl-rich acid polysaccharides originating from microbial-derived exopolymeric substances are suggested to template the growth of high aspect-ratio (nano)mineral phases.[16−18] This may proceed through an initially strong binding of dissolved Fe(III) by carboxyl groups, which is later released as the iron polymerizes and nucleation of crystalline mineral phases on the organic structure begins.[16,17] In Fh-PGA and Fh-CA, it is plausible that the excess of free solid-associated carboxyl groups interacted with the low concentrations of dissolved Fe(III),[8] templating the growth of crystalline mineral phases on the carboxyl-rich aggregate surface via the rapid oxidation of Fe(II). This is supported by the missing high-aspect ratio crystalline secondary minerals in Fh-GA (Figure 4F), where surface nucleation did not occur in the absence of free carboxyl groups. Particularly fast Fe(II) oxidation results in thin lepidocrocite sheets which tend to crumple,[60,63−65] thus comparing the (<10 nm) lepidocrocite lamina of Fh-CA to the thicker (20−60 nm) lamina of Fh-PGA indicates that Fe(II) oxidation occurred more rapidly for Fh-CA than Fh-PGA (Figure 4D−F), and explains the absence of the (020) reflection in Fh-CA XRD patterns (Figure 2C). In combination with rapid lepidocrocite formation detected with XRD, EM imaging suggests that the rapid oxidation and hydrolysis of Fe(II) on the surface of the coprecipitates resulted in the encrustation of the aggregate's ferrihydrite-OM core. As Figure S10 shows, comparing secondary electron (SE) and high-angle annular dark-field (HAADF) detector images reveals the formation of a shell-like outer layer and an aggregate core in Fh-CA which is noticeably absent in the OM-free ferrihydrite. In our previous study,[8] we interpreted unexpectedly low f^{57}Fe in solution as indicative of the formation of ^{57}Fe-enriched crystalline minerals in the first 24 h of reaction between ferrihydrite-PGA coprecipitates and ^{57}Fe(II). Aided with similar Fe isotope trends in the present study (Figure 2), and reports of isotope gradients in the solid-phases of similar Fe(II)$_{\text{spike}}$ studies,[12,23,66] we suggest that the crystalline mineral shell likely comprised mostly ^{57}Fe(II). For all coprecipitates, significant ferrihydrite contributions detected at the end of the experiment despite remaining Fe(II) in solution (Figure 2) suggest that all ligands inhibited ferrihydrite transformation and lepidocrocite formation, whereby the impact was less pronounced in the carboxyl-rich PGA and CA comprising coprecipitates compared to Fh-GA.

Following this reasoning, in ferrihydrite-OM coprecipitates, an increased excess of carboxyl groups should be expected to promote Fe(II)-catalyzed mineral transformations. Previous studies on the subject, however, show the opposite to be true, whereby increased carboxyl content or C:Fe molar ratios resulted in decreased secondary mineral formation.[8,11,12] This may reflect higher aggregation tendencies or changes in net surface charge. Alternatively, this may indicate that ferrihydrite transformation in Fh-GA as well as in coprecipitates with high C:Fe molar ratios is controlled by different growth mechanisms.

Ferrihydrite Growth and Transformation in the Presence of Fe(II) and OM. Crystal growth mechanisms in Fe oxides remain unclear, and this is particularly true for ferrihydrite, due, in part, to remaining uncertainties regarding the ferrihydrite structure. Two main mechanisms are proposed to address spontaneous growth and transformation in ferrihydrite nanoparticles; (M1) classical Ostwald ripening (OR),[19,47] where larger particles grow at the expense of smaller particles, and (M2) nonclassical oriented aggregation (OA),[19,47,67] in which primary nanoparticles rearrange and align themselves through Brownian motion to achieve common crystallographic orientations, thereby forming new secondary crystals.[68] In our Fe(II)$_{\text{spike}}$ experiment, the addition of an external aqueous Fe(II) source and OM introduces two auxiliary growth mechanisms to the system; (M3) the rapid oxidation of Fe(II) on the mineral surface (as part of the "conveyer-belt" atom exchange model[69]) and (M4) templated growth associated with carboxyl-rich surfaces.[16−18] In the OM-free ferrihydrite, (M1−M3) may be active, resulting in complementary growth processes. For example, the rate of crystal growth via OR becomes small with larger ferrihydrite particles sizes (>4 nm),[19] at which time OA may become more important.[70] Above 8 nm, ferrihydrite nanoparticles are expected to transform to nanogoethite or hematite,[56,57] which may then continue to grow via OR and/or OA.

In the presence of OM, negatively charged organic functional groups disrupt Fe attachment, leading to reduced growth rates via OR at cirumneutral to slightly acidic pH.[19] In addition, changes in the particle surface charge away from the PZC of the pure mineral phase reduces rates of OA growth.[70,71] Finally, solid-phase associated OM may constrain the Brownian motion of ferrihydrite nanoparticles, sterically

DOI: 10.1021/acs.est.9b03952
Environ. Sci. Technol. 2019, 53, 13636−13647

hindering the aggregation, rotation, alignment, and attachment of particles required for crystal growth via OA.[8,72] For these reasons, it seems unlikely that OR or OA would dominate in the carboxyl-rich Fh-PGA or Fh-CA. Rather, (M3−M4) may be important; Fe(II) oxidation and crystalline mineral formation on the mineral surface is plausible, as ferrihydrite surface sites are not likely blocked by the OM,[8,9,14,73] and EM images are consistent with high aspect-ratio mineral growth in association with carboxyl-rich surfaces.[17,18,62] In contrast, Fh-GA behaves unexpectedly; forming no crystalline secondary minerals despite a surface charge similar to that of the OM-free ferrihydrite. Lacking free carboxyl groups, (M4) is not possible in Fh-GA, although growth via OR (M1) again becomes probable. In fact, increases in particle size (Figure S4) suggest that the ferrihydrite nanoparticles did grow slightly. Still, the absence of crystalline secondary mineral phases in Fe(II)-reacted Fh-GA suggests that (M2−M3) were impeded, with the most obvious culprit being the solid-associated organic fraction. Ligand exchange between the single GA-carboxyl group and ferrihydrite-Fe positions the remaining GA structure, a pyranose ring (Figure S1), outward onto a surface, rendering it an obstructive impediment to the free movement, alignment, and attachment of nanoparticles thereby hindering successful OA growth (M2).

At the same time, it is now abundantly clear that the ferrihydrite-OM core also undergoes atom exchange (Figure S6),[8,9,12] indicating that not only electron transfer[74] occurs through the entirety of a ferrihydrite-OM aggregate. Rather, the Fe(II) adsorption, oxidation, and dissolution processes that drive atom exchange must also proceed throughout the ferrihydrite-OM aggregate core as well. For Fh-PGA and Fh-CA, the presence of negatively charged functional groups in the aggregate core may have facilitated the diffusion of Fe(II) through the aggregate, thereby increasing the rates of iron atom exchange compared to Fh-GA's slightly positively charged surfaces at pH 7 (Figure S6). Following this reasoning, the free carboxyl groups in the aggregate core of Fh-PGA and Fh-CA should have also templated the growth of crystalline minerals.[16,17] However, because dissolved Fe(III) is expected in such low concentrations,[8] it seems unlikely that this would also be present in the aggregate core; rather any dissolved Fe(III) may be rapidly complexed by surface or near-surface carboxyl groups, leading to the shell-like crust. In addition, if, during coprecipitation, the residual organic structure is rendered relatively immobile due to complexation of (at least) one of its carboxyl groups with the ferrihydrite-Fe, then free nanoparticle movement and aggregation may be hindered, as discussed above. Logically, it would follow that the impact of such surface obstructions would become more noticeable with their increasing proximity, potentially explaining why ferrihydrite persists in the aggregate core of all the coprecipitates.

Environmental Implications. Trends in iron isotope composition of the presented study concur with others works[8,9,12] showing that ferrihydrite, even in the presence of OM, actively partakes in atom exchange, sometimes resulting in drastic mineral and morphologic changes to the aggregate structure. The extent to which mineral transformations occur in ferrihydrite-OM coprecipitates appears to be contingent on the presence of free carboxyl groups, which form carboxyl-rich surfaces potentially important to templating mineral growth via Fe(II) oxidation and hydrolosis.[16,17] In the ferrihydrite-OM coprecipitates, in the absence of free carboxyl groups, no crystalline minerals were formed. Atom exchange kinetics are likely influenced by a number of factors, including particle size, SSA, and variations in nanoparticle structure. Some of these effects may be related to C content of the coprecipitate; in fact, it is known that isotope n by the sum of the totalisotope n by the sum of the totalvarying C:Fe in addition to $Fe(II)_{spike}$:Fe(III) molar ratios greatly influence ferrihydrite transformation kinetics and end-products.[8,9,11] However, in this study, we show that, given similar C:Fe molar ratios, chemical characteristics of the coprecipitating organic ligand are important; inducing changes to particle surface charge and the distribution of organic functional groups[12] which appear to control iron atom exchange kinetics as well as transformation products.

The formation of a crystalline mineral shell around a ferrihydrite-aggregate core raises the question of how "dynamic" OM-associated ferrihydrite may be under prolonged reducing conditions, and what impact this may have on ferrihydrite-OM associated trace metal(loid)s. Crystalline minerals are less prone to (a)biotic dissolution compared to poorly crystalline ferrihydrite, and thus the formation of a crystalline shell has implications for assessing the stability and microbial availability of ferrihydrite-Fe. Goethite encrusted ferrihydrite has been reported in anoxic freshwater pond sediments, where the incomplete reduction of ferrihydrite was attributed to its microbial inaccessibility rather than a lack of organic substrate.[75] This suggests that a ferrihydrite-OM core encrusted by lepidocrocite and/or goethite may promote the preservation of ferrihydrite and ferrihydrite-associated C or trace metal(loid)s. Because encrustation appears to be associated with EPS-like carboxyl-rich OM,[16,18,62] environments with predominantly microbially derived OM, such as freshwater flocs, may promote the preservation of ferrihydrite, therefore explaining why exposure to Fe(II) did not result in the release of ferrihydrite/lepidocrocite-adsorbed As in Fe-rich, organic flocs[8,9] as would be expected during (microbial) dissolution of As-bearing ferrihydrites.

■ ASSOCIATED CONTENT

Ⓢ Supporting Information

The Supporting Information is available free of charge on the ACS Publications website at DOI: 10.1021/acs.est.9b03952.

> Details to experimental materials and setup, tables of Fe isotope and XRD data, additional XRD and XAS data, and EM images (PDF)

■ AUTHOR INFORMATION

Corresponding Author

*E-mail: laurel.thomas@usys.ethz.ch.

ORCID

Laurel K. ThomasArrigo: 0000-0002-6758-3760
Ralf Kaegi: 0000-0002-2430-4733
Ruben Kretzschmar: 0000-0003-2587-2430

Notes

The authors declare no competing financial interest.

■ ACKNOWLEDGMENTS

We are grateful to K. Barmettler, S. Heller, M. Plötze, A. Röthlisberger, and M. Rothaupt (ETH Zurich) for assisting with laboratory analyses. We acknowledge ELETTRA for the provision of synchrotron radiation facilities and thank G. Aquilanti (ELETTRA, XAFS beamline) for her support during the synchrotron measurements. We acknowledge the Scientific

Center for Optical and Electron Microscopy (ScopeM) of the ETH Zurich for providing access to their microscopes. This work was funded by ETH Zürich.

■ REFERENCES

(1) Eusterhues, K.; Wagner, F. E.; Häusler, W.; Hanzlik, M.; Knicker, H.; Totsche, K. U.; Kögel-Knabner, I.; Schwertmann, U. Characterization of ferrihydrite-soil organic matter coprecipitates by X-ray diffraction and Mössbauer spectroscopy. *Environ. Sci. Technol.* **2008**, *42*, 7891−7897.

(2) Schwertmann, U.; Wagner, F.; Knicker, H. Ferrihydrite-humic associations: Magnetic hyperfine interactions. *Soil Sci. Soc. Am. J.* **2005**, *69*, 1009−1015.

(3) Shimizu, M.; Zhou, J.; Schröder, C.; Obst, M.; Kappler, A.; Borch, T. Dissimilatory reduction and transformation of ferrihydrite-humic acid coprecipitates. *Environ. Sci. Technol.* **2013**, *47*, 13375−13384.

(4) Cooper, R. E.; Eusterhues, K.; Wegner, C. E.; Totsche, K. U.; Küsel, K. Ferrihydrite-associated organic matter (OM) stimulates reduction by *Shewanella oneidensis* MR-1 and a complex microbial consortia. *Biogeosciences* **2017**, *14*, 5171−5188.

(5) Mikutta, C.; Mikutta, R.; Bonneville, S.; Wagner, F.; Voegelin, A.; Christl, I.; Kretzschmar, R. Synthetic coprecipitates of exopolysaccharides and ferrihydrite. Part 1: Characterization. *Geochim. Cosmochim. Acta* **2008**, *72*, 1111−1127.

(6) Kleber, M.; Eusterhues, K.; Kueiluweit, M.; Mikutta, C.; Mikutta, R.; Nico, P. S. Mineral-organic associations: Formation, properties, and relevance in soil environments. In *Advances in Agronomy*; Sparks, D. L., Ed.; Academic Press: 2015.

(7) Pan, W. N.; Kan, J.; Inamdar, S.; Chen, C. M.; Sparks, D. Dissimilatory microbial iron reduction release DOC (dissolved organic carbon) from carbon-ferrihydrite association. *Soil Biol. Biochem.* **2016**, *103*, 232−240.

(8) ThomasArrigo, L. K.; Byrne, J. M.; Kappler, A.; Kretzschmar, R. Impact of organic matter on iron(II)-catalyzed mineral transformation in ferrihydrite-OM coprecipitates. *Environ. Sci. Technol.* **2018**, *52*, 12316−12326.

(9) ThomasArrigo, L. K.; Mikutta, C.; Byrne, J.; Kappler, A.; Kretzschmar, R. Iron(II)-catalyzed iron atom exchange and mineralogical changes in iron-rich organic freshwater flocs: An iron isotope tracer study. *Environ. Sci. Technol.* **2017**, *51*, 6897−6907.

(10) Jones, A. M.; Collins, R. N.; Rose, J.; Waite, T. D. The effect of silica and natural organic matter on the Fe(II)-catalysed transformation and reactivity of Fe(III) minerals. *Geochim. Cosmochim. Acta* **2009**, *73*, 4409−4422.

(11) Chen, C.; Kukkadapu, R. K.; Sparks, D. L. Influence of coprecipitated organic matter on $Fe^{2+}{}_{(aq)}$-catalyzed transformation of ferrihydrite: Implications for carbon dynamics. *Environ. Sci. Technol.* **2015**, *49*, 10927−10936.

(12) Zhou, Z.; Latta, D. E.; Noor, N.; Thompson, A.; Borch, T.; Scherer, M. M. Fe(II)-catalyzed transformation of organic matter-ferrihydrite coprecipitates: A closer look using Fe isotopes. *Environ. Sci. Technol.* **2018**, *52*, 11142−11150.

(13) Henneberry, Y. K.; Kraus, T. E. C.; Nico, P. S.; Horwath, W. R. Structural stability of coprecipitated natural organic matter and ferric iron under reducing conditions. *Org. Geochem.* **2012**, *48*, 81−89.

(14) ThomasArrigo, L. K.; Mikutta, C.; Lohmayer, R.; Planer-Friedrich, B.; Kretzschmar, R. Sulfidization of organic freshwater flocs from a minerotrophic peatland: Speciation changes of iron, sulfur, and arsenic. *Environ. Sci. Technol.* **2016**, *50*, 3607−3616.

(15) Poulton, S. W.; Krom, M. D.; Raiswell, R. A revised scheme for the reactivity of iron (oxyhydr)oxide minerals towards dissolved sulfide. *Geochim. Cosmochim. Acta* **2004**, *68*, 3703−3715.

(16) Chan, C. S.; De Stasio, G.; Welch, S. A.; Girasole, M.; Frazer, B. H.; Nesterova, M. V.; Fakra, S.; Banfield, J. F. Microbial polysaccharides template assembly of nanocrystal fibers. *Science* **2004**, *303*, 1656−1658.

(17) Chan, C. S.; Fakra, S. C.; Edwards, D. C.; Emerson, D.; Banfield, J. F. Iron oxyhydroxide mineralization on microbial extracellular polysaccharides. *Geochim. Cosmochim. Acta* **2009**, *73*, 3807−3818.

(18) Chan, C. S.; Fakra, S. C.; Emerson, D.; Fleming, E. J.; Edwards, K. J. Lithotrophic iron-oxidizing bacteria produce organic stalks to control mineral growth: implications for biosignature formation. *ISME J.* **2011**, *5*, 717−727.

(19) Hiemstra, T.; Mendez, J.; Li, J. Evolution of the reactive surface area of ferrihydrite: time, pH, and temperature dependency of growth by Ostwald ripening. *Environ. Sci.: Nano* **2019**, *6*, 820−833.

(20) Mikutta, C. X-ray absorption spectroscopy study on the effect of hydroxybenzoic acids on the formation and structure of ferrihydrite. *Geochim. Cosmochim. Acta* **2011**, *75*, 5122−5139.

(21) Mikutta, C.; Frommer, J.; Voegelin, A.; Kaegi, R.; Kretzschmar, R. Effect of citrate on the local Fe coordination in ferrihydrite, arsenate binding, and ternary arsenate complex formation. *Geochim. Cosmochim. Acta* **2010**, *74*, 5574−5592.

(22) Pedersen, H. D.; Postma, D.; Jakobsen, R.; Larsen, O. Fast transformation of iron oxyhydroxides by the catalytic action of aqueous Fe(II). *Geochim. Cosmochim. Acta* **2005**, *69*, 3967−3977.

(23) Southall, S. C.; Micklethwaite, S.; Wilson, S. A.; Frierdich, A. J. Changes in crystallinity and tracer-isotope distribution of goethite during Fe(II)-accelerated recrystallization. *ACS Earth Space Chem.* **2018**, *2*, 1271−1282.

(24) Frierdich, A. J.; Helgeson, M.; Liu, C.; Wang, C.; Rosso, K. M.; Scherer, M. M. Iron atom exchange between hematite and aqueous Fe(II). *Environ. Sci. Technol.* **2015**, *49*, 8479−8486.

(25) Pasakarnis, T.; McCormick, M. L.; Parkin, G. F.; Thompson, A.; Scherer, M. M. $Fe^{II}{}_{aq}$-$Fe^{III}{}_{oxide}$ electron transfer and Fe exchange: Effect of organic carbon. *Environ. Chem.* **2015**, *12*, 52−63.

(26) Chen, C.; Sparks, D. L. Fe(II)-induced mineral transformation of ferrihydrite-organic matter adsorption and co-precipitation complexes in the absence and presence of As(III). *ASC Earth Space Chem.* **2018**, *2*, 1095−1101.

(27) ThomasArrigo, L. K.; Mikutta, C.; Byrne, J.; Barmettler, K.; Kappler, A.; Kretzschmar, R. Iron and arsenic speciation and distribution in organic flocs from streambeds of an arsenic-enriched peatland. *Environ. Sci. Technol.* **2014**, *48*, 13218−13228.

(28) Daugherty, E. E.; Gilbert, B.; Nico, P. S.; Borch, T. Complexation and redox buffering of iron(II) by dissolved organic matter. *Environ. Sci. Technol.* **2017**, *51*, 11096−11104.

(29) Schwertmann, U.; Cornell, R. M. *Iron Oxides in the Laboratory: Preparation and Characterization*; WILEY-VCH Verlag GMBH & Co. KGaA: Weinheim, Germany, 2000.

(30) Hofmann, A.; Pelletier, M.; Michot, L.; Stradner, A.; Schurtenberger, P.; Kretzschmar, R. Characterization of the pores in hydrous ferric oxide aggregates formed by freezing and thawing. *J. Colloid Interface Sci.* **2004**, *271*, 163−173.

(31) Mikutta, R.; Mikutta, C. Stabilization of organic matter at micropores (<2 nm) in acid forest subsoils. *Soil Sci. Soc. Am. J.* **2006**, *70*, 2049−2056.

(32) Scarlett, N. V. Y.; Madsen, I. C. Quantification of phases with partial or no known crystal structures. *Powder Diffr.* **2006**, *21*, 278−284.

(33) Aeppli, M.; Kaegi, R.; Kretzschmar, R.; Voegelin, A.; Hofstetter, T. B.; Sander, M. Electrochemical analysis of changes in iron oxide reducibility during abiotic ferrihydrite transformation into goethite and magnetite. *Environ. Sci. Technol.* **2019**, *53*, 3568−3578.

(34) Fortune, W. B.; Mellon, M. G. Determination of iron with *o*-phenanthroline - A spectrophotometric study. *Ind. Eng. Chem., Anal. Ed.* **1938**, *10*, 60−64.

(35) Taylor, P. D. P.; Maeck, R.; Debievre, P. Determination of the absolute isotopic composition and atomic weight of a reference sample of natural iron. *Int. J. Mass Spectrom. Ion Processes* **1992**, *121*, 111−125.

(36) Ravel, B.; Newville, M. ATHENA, ARTEMIS, HEPHAESTUS: data analysis for X-ray absorption spectroscopy using IFEFFIT. *J. Synchrotron Radiat.* **2005**, *12*, 537−541.

DOI: 10.1021/acs.est.9b03952

(37) Zabinsky, S. I.; Rehr, J. J.; Ankudinov, A.; Albers, R. C.; Eller, M. J. Multiple-scattering calculations of X-ray absorption spectra. *Phys. Rev. B: Condens. Matter Mater. Phys.* **1995**, *52*, 2995−3009.

(38) Kaur, N.; Singh, B.; Kennedy, B. J.; Gräfe, M. The preparation and characterization of vanadium-substituted goethite: The importance of temperature. *Geochim. Cosmochim. Acta* **2009**, *73*, 582−593.

(39) Zhukhlistov, A. P. Crystal structure of lepidocrocite FeO(OH) from the electron-diffractometry data. *Crystallogr. Rep.* **2001**, *46*, 730−733.

(40) Gu, B. H.; Schmitt, J.; Chen, Z. H.; Liang, L. Y.; McCarthy, J. F. Adsorption and desorption of natural organic matter on iron oxide: Mechanisms and models. *Environ. Sci. Technol.* **1994**, *28*, 38−46.

(41) Hansel, C. M.; Wielinga, B. W.; Fendorf, S. Structural and compositional evolution of Cr/Fe solids after indirect chromate reduction by dissimilatory iron-reducing bacteria. *Geochim. Cosmochim. Acta* **2003**, *67*, 401−412.

(42) Waychunas, G. A.; Rea, B. A.; Fuller, C. C.; Davis, J. A. Surface chemistry of ferrihydrite: Part 1. EXAFS studies of the geometry of coprecipitated and adsorbed arsenate. *Geochim. Cosmochim. Acta* **1993**, *57*, 2251−2269.

(43) Manceau, A. Critical evaluation of the revised akdalaite model for ferrihydrite. *Am. Mineral.* **2011**, *96*, 521−533.

(44) Voegelin, A.; Kaegi, R.; Frommer, J.; Vantelon, D.; Hug, S. J. Effect of phosphate, silicate, and Ca on Fe(III)-precipitates formed in aerated Fe(II)- and As(III)-containing water studied by X-ray absorption spectroscopy. *Geochim. Cosmochim. Acta* **2010**, *74*, 164−186.

(45) Wang, X. M.; Zhu, M. Q.; Koopal, L. K.; Li, W.; Xu, W. Q.; Liu, F.; Zhang, J.; Liu, Q. S.; Feng, X. H.; Sparks, D. L. Effects of crystallite size on the structure and magnetism of ferrihydrite. *Environ. Sci.: Nano* **2016**, *3*, 190−202.

(46) Hiemstra, T. Surface and mineral structure of ferrihydrite. *Geochim. Cosmochim. Acta* **2013**, *105*, 316−325.

(47) Hiemstra, T. Surface structure controlling nanoparticle behavior: magnetism of ferrihydrite, magnetite, and maghemite. *Environ. Sci.: Nano* **2018**, *5*, 752−764.

(48) Michel, F. M.; Ehm, L.; Antao, S. M.; Lee, P. L.; Chupas, P. J.; Liu, G.; Strongin, D. R.; Schoonen, M. A. A.; Phillips, B. L.; Parise, J. B. The structure of ferrihydrite, a nanocrystalline material. *Science* **2007**, *316* (5832), 1726−1729.

(49) Elliott, A. V. C.; Plach, J. M.; Droppo, I. G.; Warren, L. A. Collaborative microbial Fe-redox cycling by pelagic floc bacteria across wide ranging oxygenated aquatic systems. *Chem. Geol.* **2014**, *366*, 90−102.

(50) Joshi, P.; Gorski, C. A. Anisotropic morphological changes in goethite during Fe^{2+}-catalyzed recrystallization. *Environ. Sci. Technol.* **2016**, *50*, 7315−7324.

(51) Handler, R. M.; Beard, B. L.; Johnson, C. M.; Scherer, M. M. Atom exchange between aqueous Fe(II) and goethite: An Fe isotope tracer study. *Environ. Sci. Technol.* **2009**, *43*, 1102−1107.

(52) Handler, R. M.; Frierdich, A. J.; Johnson, C. M.; Rosso, K. M.; Beard, B. L.; Wang, C.; Latta, D. E.; Neumann, A.; Pasakarnis, T.; Premaratne, W. A. P. J.; Scherer, M. M. Fe(II)-catalyzed recrystallization of goethite revisited. *Environ. Sci. Technol.* **2014**, *48*, 11302−11311.

(53) Hochella, M. F.; Lower, S. K.; Maurice, P. A.; Penn, R. L.; Sahai, N.; Sparks, D. L.; Twining, B. S. Nanominerals, mineral nanoparticles, and Earth systems. *Science* **2008**, *319* (5870), 1631−1635.

(54) Cismasu, A. C.; Michel, F. M.; Tcaciuc, A. P.; Tyliszczak, T.; Brown, G. E., Jr Composition and structural aspects of naturally occurring ferrihydrite. *C. R. Geosci.* **2011**, *343*, 210−218.

(55) Janney, D. E.; Cowley, J. M.; Buseck, P. R. Transmission electron microscopy of synthetic 2-and 6-line ferrihydrite. *Clays Clay Miner.* **2000**, *48*, 111−119.

(56) Hiemstra, T. Formation, stability, and solubility of metal oxide nanoparticles: Surface entropy, enthalpy, and free energy of ferrihydrite. *Geochim. Cosmochim. Acta* **2015**, *158*, 179−198.

(57) Navrotsky, A.; Mazeina, L.; Majzlan, J. Size-driven structural and thermodynamic complexity in iron oxides. *Science* **2008**, *319* (5870), 1635−1638.

(58) Yanina, S. V.; Rosso, K. M. Linked reactivity at mineral-water interfaces through bulk crystal conduction. *Science* **2008**, *320*, 218−222.

(59) Gorski, C. A.; Handler, R. M.; Beard, B. L.; Pasakarnis, T.; Johnson, C. M.; Scherer, M. M. Fe atom exchange between aqueous Fe^{2+} and magnetite. *Environ. Sci. Technol.* **2012**, *46*, 12399−12407.

(60) Cornell, R. M.; Schwertmann, U. *The Iron Oxides: Structure, Properties, Reactions, Occurances and Uses*; Wiley-VCH: Weinheim, Germany, 2003.

(61) Alcántara, J.; Chico, B.; Simancas, J.; Díaz, I.; de la Fuente, D.; Morcillo, M. An attempt to classify the morphologies presented by different rust phases formed during the exposure of carbon steel to marine atmospheres. *Mater. Charact.* **2016**, *118*, 65−78.

(62) Byrne, J. M.; Schmidt, M.; Gauger, T.; Bryce, C.; Kappler, A. Imaging organic-mineral aggregates formed by Fe(II)-oxidizing bacteria using helium ion microscopy. *Environ. Sci. Technol. Lett.* **2018**, *5*, 209−213.

(63) Kassim, J.; Baird, T.; Fryer, J. R. Electron microscope studies of iron corrosion products in water at room-temperature. *Corros. Sci.* **1982**, *22*, 147−158.

(64) Mackenzie, R. C.; Meldau, R. Aeging of sesquioxide gels. *Mineral. Mag. J. Mineral. Soc.* **1959**, *32*, 153−165.

(65) Schwertmann, U.; Thalmann, H. The influence of [Fe(II)], [Si], and pH on the formation of lepidocrocite and ferrihydrite during oxidation of aqueous $FeCl_2$ solutions. *Clay Miner.* **1976**, *11*, 189−200.

(66) Taylor, S. D.; Liu, J.; Arey, B. W.; Schreiber, D. K.; Perea, D. E.; Rosso, K. M. Resolving iron(II) sorption and oxidative growth on hematite (001) using Atom Probe Tomography. *J. Phys. Chem. C* **2018**, *122*, 3903−3914.

(67) Li, D. S.; Nielsen, M. H.; Lee, J. R. I.; Frandsen, C.; Banfield, J. F.; De Yoreo, J. J. Direction-Specific Interactions Control Crystal Growth by Oriented Attachment. *Science* **2012**, *336* (6084), 1014−1018.

(68) Penn, R. L. Kinetics of oriented aggregation. *J. Phys. Chem. B* **2004**, *108*, 12707−12712.

(69) Boland, D.; Collins, R.; Miller, C.; Glover, C.; Waite, T. D. Effect of solution and solid-phase conditions on the Fe(II)-accelerated transformation of ferrihydrite to lepidocrocite and goethite. *Environ. Sci. Technol.* **2014**, *48*, 5477−5485.

(70) Burleson, D. J.; Penn, R. L. Two-step growth of goethite from ferrihydrite. *Langmuir* **2006**, *22*, 402−409.

(71) Penn, R. L.; Banfield, J. F. Imperfect oriented attachment: Dislocation generation in defect-free nanocrystals. *Science* **1998**, *281*, 969−971.

(72) Kennedy, C. B.; Scott, S. D.; Ferris, F. G. Hydrothermal phase stabilization of 2-line ferrihydrite by bacteria. *Chem. Geol.* **2004**, *212*, 269−277.

(73) Chen, C. M.; Dynes, J. J.; Wang, J.; Sparks, D. L. Properties of Fe-organic matter associations via coprecipitation versus adsorption. *Environ. Sci. Technol.* **2014**, *48*, 13751−13759.

(74) Soltis, J. A.; Schwartzberg, A. M.; Zarzycki, P.; Penn, R. L.; Rosso, K. M.; Gilbert, B. Electron mobility and trapping in ferrihydrite nanoparticles. *ASC Earth Space Chem.* **2017**, *1*, 216−226.

(75) Kikuchi, S.; Makita, H.; Konno, U.; Shiraishi, F.; Ijiri, A.; Takai, K.; Maeda, M.; Takahashi, Y. Limited reduction of ferrihydrite encrusted by goethite in freshwater sediment. *Geobiol.* **2016**, *14* (4), 374−389.

(76) Kelly, S. D.; Hesterberg, D.; Ravel, B. Analysis of soils and minerals using X-ray absorption spectroscopy. In *Methods of Soil Analysis. Part 5. Minerological Methods*; Ulery, A. L., Drees, L. R., Eds.; Soil Science Society of America: Madison, 2008; pp 378−463.

DOI: 10.1021/acs.est.9b03952